

RETRIEVAL OF HORIZONTAL WIND PERTURBATION FIELDS FROM SIMULATED SINGLE DOPPLER RADAR OBSERVATIONS *

Gu Songshan (顾松山)

Nanjing Institute of Meteorology, Nanjing 210044

I. Zawadzki and S. Laroche

Departement de physique, Universite du Quebec a Montreal Canada, H3P 3P8

Received January 10, 1993; revised August 10, 1993

ABSTRACT

The application of the single Doppler radar dataset analysis is usually confined to the assumption that the actual wind is linearly distributed or uniform locally. Following some dynamic features of convective weather, a conceptual model of moderate complexity is constructed, wherewith a horizontal wind perturbation field is retrieved directly from the single Doppler radar measurements. The numerical experiments are based on a 3-D cloud model-generated convective cell, whose radial velocity component is taken as the radar observations that are put into the closed equations based on the conceptual model to retrieve the horizontal wind perturbation field. After the initial field is properly treated, the retrieval equation is solved in terms of the 2-D FFT technique and the sensitivity to noise is examined. Finally, contrast analysis is done of the retrieved and the cloud model output wind fields, indicating the usefulness of the approach proposed in this paper.

Key words: Doppler radar, FFT technique, retrieval wind field

1. INTRODUCTION

During the past 25 years significant advances have been made with single-Doppler radar analysis of mesoscale research and forecasting. The achievements are so attractive that major commitment has been made to install Doppler radar networks in operational weather services in several countries.

However, a major disadvantage of single Doppler radar is that it measures only, the velocity component directed toward or away from the radar. Since the measurements are incomplete for a comprehensive description of the actual wind field, an effort has to be made to obtain information on the other wind components. The interpretation of single Doppler velocities is usually based on either the signatures of various phenomena of interest, the tracking of reflectivity or velocity features, or on simple assumptions such as the linear dependence of wind components (U , V) on the coordinates (x , y).

The tracking of echo or velocity patterns employs techniques of pattern recognition using cross-correlation analysis. Tuttle and Foote (1990) explored further the potential of using the technique on clear air echoes and described a method for determining the airflow in the

* The study is supported by the National Natural Science Foundation of China.

boundary layer using clear-air return from a single Doppler radar. As indicated by the authors the mean winds are only estimated by determining, via correlation calculations, the displacement of these patterns between successive scans.

The assumptions of a linearly varying wind field in space and time invariant over the scan interval have been used extensively in single Doppler analysis. This is the case for the velocity azimuth display (VAD) method, the velocity area display (VARD) method and the modified VVP (MVVP) method. In particular, the least square VAD method has been used successfully in an operational mode. Based upon the MVVP method, Johnston and Marwitz (1990) developed a new analysis method specifically designed for banded precipitation structures that exhibit a high degree of two-dimensionality, the vorticity contamination of the horizontal velocity components can be effectively rejected using symmetry of banded precipitation.

Although the VAD, VVP methods and their variations provide useful information on the vertical profile of the kinematic structure, they have major limitations. First, the analysis volume must be fairly large, such that a sufficient sample statistics can be obtained. This makes it difficult to achieve the resolution necessary to examine the kinematic structure of small-scale severe weather systems. Also, the farther away from the radar station, the lower the resolution is. Perhaps it is most important that linearity assumptions may not be appropriated the scales on which the analysis is made. The assumption of a linear wind field constrains the perturbation field of vorticity and divergence to be zero. Yet features such as mesocyclones or divergent outflows can be identified by eye on a color display of the radial velocity. These features are clearly related to the perturbation fields of divergence and vorticity. This example suggests that the assumption of linearity is over-restrictive. Although based on MVVP method after computing the wind speed and direction in a number of proximal areas, the vorticity and divergence can be calculated, the reliability for the perturbation field that one computes via this technique has not been demonstrated. Intuitively it is not clear why a technique that is based on the assumption of a uniform wind should yield reliable estimates of perturbation fields (Passarelli 1983).

To further utilize the data, a meteorologist must be able to infer some information about the other wind components and the cross-beam winds possibly by means of the thermodynamic properties, pressure and temperature. Recently the retrieval of the 3-D wind and temperature fields was explored using the simulated single-Doppler radial velocity in conjunction with the full set of differential equations governing the atmospheric motions (Sun et al. 1991). It is shown that the method is able to determine the spatial structures of the unobserved velocity components and temperature effectively. But there is a wide conceptual and theoretical gap between the approach of Sun et al. and previous methods of Doppler data interpretation.

A method to find the horizontal wind perturbation fields from single-Doppler radar data would benefit meteorologists concerned with small-scale flows and other users of the Doppler radar products. In this work we explore a method of intermediate complexity, in which some known properties of airflow are introduced through a semi-quantitative conceptual model. This paper describes a technique for evaluating vertical component of the perturbation fields of vorticity and horizontal components of the perturbation of divergence from a time series of observations of a single radial velocity component via closure equations, which depend upon the semi-quantitative conceptual model. The closure equations are solved by 2-D FFT in a limited regions. The potential of the method is demonstrated.

The retrieval method presented here will be tested in simulated convection using a 3-D cloud model. The advantage of this approach is that the actual wind field is completely known. Thus a number of sensitivity tests can be readily performed and the results can be compared to the known truth.

The following sections give a physical and a mathematical specification of the problem, describe the retrieval equations, the method of solution, single processing and show results. The concluding section outlines steps that remain to make the method operational.

II. SPECIFICATION OF THE CONCEPTUAL MODEL

1. *Physical Conception*

Let us consider low elevation angles so that the Doppler velocity can be associated with the radial velocity (V_r) of the horizontal wind field. Then, only one relationship between the tangential velocity, V_p , and V_r is needed for the retrieval of the horizontal wind field. Without appealing to the complex set of dynamic equations a general relationship between V_r and V_p does not exist. However, in somehow configurations approximate relationship may hold. Of particular interest here is the correlation of the field of vorticity (ζ) and divergence (D) in convective situations.

This relationship between D and ζ results from the tilting of the ambient wind shear by the convective currents and has been discussed theoretically (Lilly 1986) and observed in nature with dual Doppler radar (Ray 1976).

However, a relationship between ζ and D establishes a relationship between the derivatives of V_r and V_p , and this is not sufficient to retrieve V_p unless either boundary conditions are specified or a functional form is assumed for the wind field. Based on the above observational facts and theoretical findings a closed equation set is established for retrieving V_p .

2. *Convective Model*

The convection situation was simulated using the Steiner-Yan model. The version of the model used here, described by Yan and Michaud (1982), permits the simulation of a field of clouds initiated by a random heating at ground superimposed to a steady increase of temperature. A $32 \times 32 \times 6$ km domain was used with 1 km grid spacing in the horizontal and 300 m in the vertical dimensions. Otherwise the conditions are the same as in Yan and Michaud.

3. *Closure Equation*

In the Cartesian coordinate system vertical vorticity ζ is in the form

$$\zeta = \frac{\partial v}{\partial x} - \frac{\partial u}{\partial y}.$$

Since the observed relationship between the fields of D and ζ is mainly due to the tilting of the vorticity associated with the horizontal wind shear we express this relationship as

$$\zeta = \alpha \mathbf{k} \cdot (\mathbf{u}_z \times \nabla D), \quad (1)$$

here \mathbf{u}_z is the wind shear vector, α is the coefficient and \mathbf{k} is the unit vector in the vertical direction. Figure 1 shows the fields of divergence and vorticity calculated by a spectral method at 3.75 km level after 106 minutes of simulation time. The characteristic duplet of vorticity is associated with the region of strong divergence. Equation (1) captures well the alignment of the

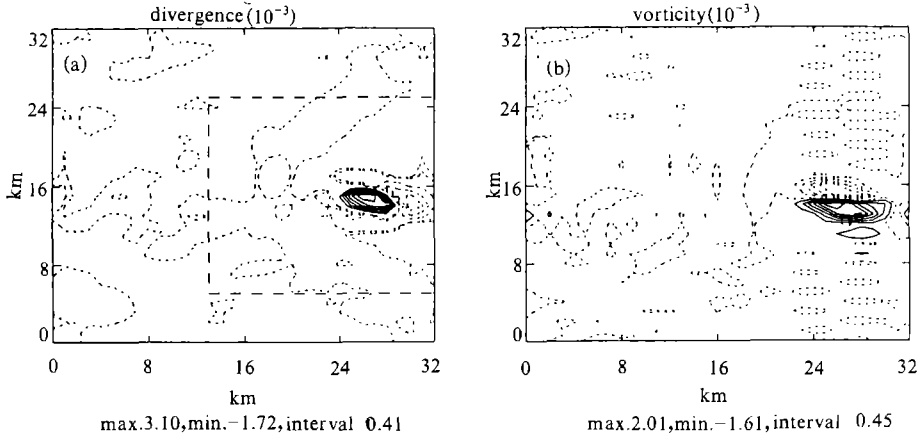


Fig. 1. Fields of divergence and vorticity in the model output at 3.75 km height and after 106 min of simulation time, which are calculated by a spectral method in Cartesian coordinate system.

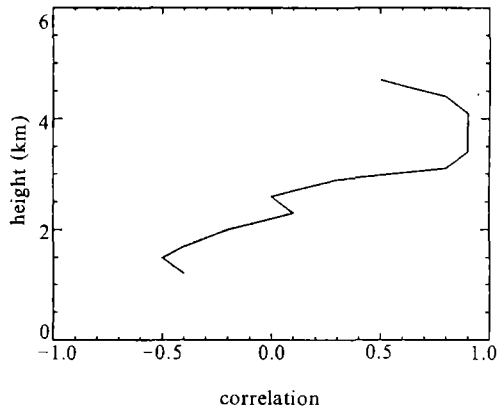


Fig. 2. Correlation coefficient between the actual vorticity and the vorticity given by the closure Eq. (1) as a function of height.

two vorticity maxima perpendicular to the direction of the wind shear and the correspondence of vorticity maxima to the region where divergence changes rapidly with distance. Figure 2 shows the correlation coefficient ρ between the actual vorticity in the model output and the vorticity derived from Eq. (1) after 106 minutes of simulation time. The change in sign of ρ is due to the change in sign of D as the flow changes from convergent to divergent while the sign of vorticity remains the same.

III. RETRIEVAL EQUATIONS

It is important to design a retrieval equation based on the semi-quantitative conceptual model (Eq. 1). The matter boils down to resolving a partial differential equation with unknown boundary conditions. Usually, it is a Taylor-Fourier expansion of (U, V) as function of (x, y) with radar station located at the center (Laroche and Zawadzki, 1988). In fact, local severe

convective activity changes quickly in space and time. In the frequency domain that means, a large quantity of waves of high wave numbers is present. Its size is limited with very strong local inhomogeneity. It does not always include the origin of coordinate (the radar station). Therefore, a reasonable method is a 2-D Fourier transform in limited regions. It takes into account the contribution from waves of all different wavelengths. This method makes it possible for the data processed to be closer to the real features of actual wind field.

For simplicity, however, the radar coordinate system will still be referred to as polar coordinate. It is to be noted that φ -direction in radar coordinate system is opposite to that in general polar coordinate system. In the following we will develop the retrieval equations based on the above semi-quantitative conceptual model using the 2-D Fourier transform over a limited domain.

In polar coordinates, vorticity, divergence and vertical wind shear vector are expressed as

$$\zeta = -\frac{V_\varphi}{r} - \frac{\partial V_\varphi}{\partial r} + \frac{1}{r} \frac{\partial V_r}{\partial \varphi}, \quad (2)$$

$$D = \frac{1}{r} \left(\frac{\partial r V_r}{\partial r} + \frac{\partial V_\varphi}{\partial \varphi} \right) = \frac{V_r}{r} + \frac{\partial V_r}{\partial r} + \frac{1}{r} \frac{\partial V_\varphi}{\partial \varphi}, \quad (3)$$

$$\mathbf{u}_z = U_z \mathbf{r} + V_z \varphi, \quad A = U_z \sin \varphi + V_z \cos \varphi, \quad B = U_z \cos \varphi - V_z \sin \varphi,$$

where U_z and V_z are the vertical shear components of the horizontal wind field, respectively.

Based on Eqs. (1), (2) and (3) the following equation can be derived:

$$\begin{aligned} \mathbf{k} \cdot (\mathbf{u}_z \times \nabla D) &= \frac{1}{r} \frac{\partial D}{\partial \varphi} A - \frac{\partial D}{\partial r} B \\ &- r V_\varphi - \alpha B \frac{\partial V_\varphi}{\partial \varphi} + \alpha A \frac{\partial^2 V_\varphi}{\partial \varphi^2} - r^2 \frac{\partial V_\varphi}{\partial r} + \alpha B r \frac{\partial^2 V_\varphi}{\partial r \partial \varphi} \\ &= -r \frac{\partial V_r}{\partial \varphi} - \alpha A \frac{\partial^2 r V_r}{\partial r \partial \varphi} + \alpha B \frac{\partial r V_r}{\partial r} - \alpha B r \frac{\partial^2 r V_r}{\partial r^2}. \end{aligned} \quad (5)$$

All the variables in Eq. (5) are transformed into wave number domain through Fourier expansion as a function of azimuth (φ) and radius (r).

$$\begin{aligned} V_\varphi &= \sum_{mh} V_{\varphi mh} e^{i(L_m r + L_h \varphi)}, & V_r &= \sum_{mh} V_{r mh} e^{i(L_m r + L_h \varphi)}, \\ r V_r &= \sum_{mh} (r V_r)_{mh} e^{i(L_m r + L_h \varphi)}, & r &= \sum_{jk} r_{jk} e^{i(L_j r + L_k \varphi)}, \\ r^2 &= \sum_{jk} (r^2)_{jk} e^{i(L_j r + L_k \varphi)}, & A &= \sum_{jk} A_{jk} e^{i(L_j r + L_k \varphi)}, \\ B &= \sum_{jk} B_{jk} e^{i(L_j r + L_k \varphi)}, & B r^2 &= \sum_{jk} (B r^2)_{jk} e^{i(L_j r + L_k \varphi)}, \end{aligned}$$

where $L_m = \frac{2\pi}{\Delta r} m$, $L_h = \frac{2\pi}{\Delta \varphi} h$, $L_j = \frac{2\pi}{\Delta r} j$, $L_k = \frac{2\pi}{\Delta \varphi} k$. Δr and $\Delta \varphi$ are the sizes of the domain for Fourier transform. m, h, j, k are wavenumbers of the corresponding variables in wavenumber domain from $-(M-1)/2$ to $(M-1)/2$ and from $-(N-1)/2$ to $(N-1)/2$, respectively. M and N are the maximum discrete sample numbers in both r and φ directions.

We replace now a variable in Eq. (5) by its Fourier coefficient. By virtue of orthogonality of Fourier components, the transform of a product term is replaced by the convolution of the two

transforms. Next, we set the coefficient of each harmonic equal to zero by orthogonality. The following equation is obtained:

$$\begin{aligned} & \sum_{\mathbf{k}} \left[-r_{m-j, h-k} - iL_h \alpha B_{m-j, h-k} + (iL_h)^2 \alpha A_{m-j, h-k} - iL_m (rs)_{m-j, h-k} \right. \\ & \quad \left. + i^2 L_m L_h \alpha (Br)_{m-j, h-k} \right] v_{\varphi, \mathbf{k}} \\ & = - \sum_{\mathbf{k}} iL_h r_{m-j, h-k} v_{r, \mathbf{k}} + \sum_{\mathbf{k}} \left[-iL_m L_h \alpha A_{m-j, h-k} \right. \\ & \quad \left. + iL_m \alpha B_{m-j, h-k} - (iL_m)^2 \alpha (Br)_{m-j, h-k} \right] (RV)_{\mathbf{k}}. \end{aligned} \quad (6)$$

When $|m-j| > (M-1)/2$ or $|h-k| > (N-1)/2$, $A_{m-j, h-k}$, $r_{m-j, h-k}$ etc. will be out of range, the corresponding coefficient is equal to zero.

The above equation is a set of multivariate linear equations, which include all the Fourier coefficients of V_φ as unknowns. The number of equations is equal to $M \times N$. V_r can be measured directly by the radar and others are known variables except V_φ . α is a constant that should be adjusted in examination for a best estimation of V_φ field.

IV. SIGNAL PROCESSING

1. Simulated Data in Polar Coordinate System

Simulated data in polar coordinate can be determined based on the elevation angle, the accuracy of simulated data in Cartesian coordinate in space domain, and the radar antenna beam width.

As shown in Fig. 1, it is an advantage that the wind field of the 3-D cloud model used for the present study is at 3.75 km level, and therefore it is necessary that we set the center of the simulated data at least at 21 km away from center of polar coordinate as A, B, C, D shown in Fig. 3, i. e. $R > 21$ km. It makes the highest elevation of antenna scanning about 10° , and keeps velocity data from being contaminated by the falling speed of hydrometeors.

Wind velocities were interpolated from the Cartesian (model output) to the polar coordinates by a bilinear interpolation using the simulated after the domain extension as A', B', C', D' shown in Fig. 3. The wind velocities thus obtained can well represent radial velocities measured by a single Doppler radar.

To make a convenient use of FFT, the simulated wind field needs to be taken in a fan-shaped sector as EFGH shown in Fig. 3. Grid size in the fan region was determined based on the resolution of the radar antenna beam and grid size of the model output in Cartesian coordinate. Resolution of radar antenna beam and accuracy of simulated data in space domain, i. e. size of sampling in azimuth, at least, is equal to or greater than 46, should be met as simultaneously as possible. Zawadzki (1973) pointed out that in attempting to define the resolution of the radar beam one found that ability to distinguish two features in the weather system depended not only on the characteristics and the separation of the features but also on the measurement precision and the prominence of the feature with respect to the background weather. The half-power beam width is a good measure of the resolution of the radar beam. According to Gu et al. (1986), when weather echo is sampled on one third of a radar beam width in azimuth, the quality of echo picture obtained is more satisfactory. Therefore, if the radar

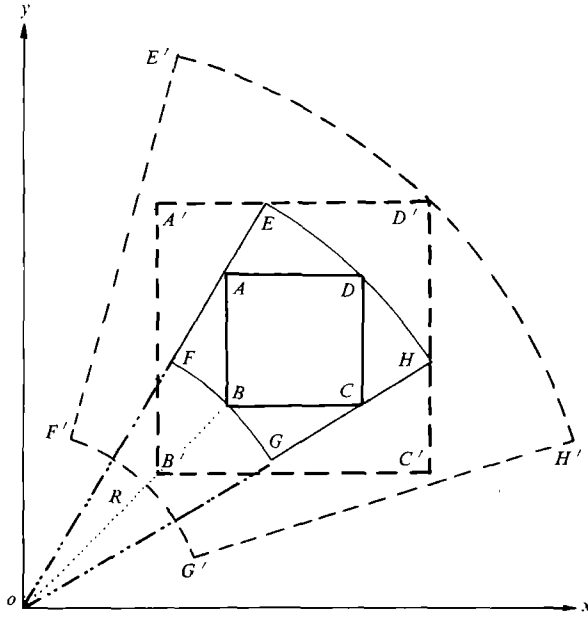


Fig. 3. Simulated data in polar coordinate system and periodic extension of domain

beam width equals to one degrees, in Fig. 3, the angle AOC, must be greater than about 15° .

2. *Gibb's Phenomenon and Filtering*

In order to solve (6) for discrete wavenumbers, operations such as convolution and differentiation are required. This makes it a nontrivial task to minimize the impact of the Gibb's phenomenon, which is inherent in the discrete spectral analyses. In regions where signals exhibit discontinuities, for example, near boundaries and at the origin of the polar coordinates, or even just in abrupt variations of the field, the true structure of the wind field is seriously distorted.

This effect, can cause ripples in fields and may also affect the amplitude of extreme. To reduce the Gibb's phenomenon, different filtering techniques have been applied to our numerical scheme. It was found that the ideal filter and Hanning window, which are often used in numerical analyses and digital signal processing, can not effectively solve the problem. Butterworth (BW) and exponential filter are more efficient but still not satisfactory in dealing with sudden jumps near the boundaries. Moreover, the latter group of filters significantly reduce the amplitudes of the signal.

Figure 4 illustrates the Gibb's phenomenon in the vorticity field calculated by discretization algorithms and its damping through different filters. Figure 4a corresponds to a section at $r = 28$ km in Fig. 1b and shows the vorticity field calculated from the Fourier expansion of wind components, (u, v) in Cartesian coordinates.

Figure 4b is as Fig. 4a except for vorticity field calculated by Eq. (2) using simulated data. In Fig. 4 a solid curve represents the unfiltered field, a dash curve shows the result with 4th

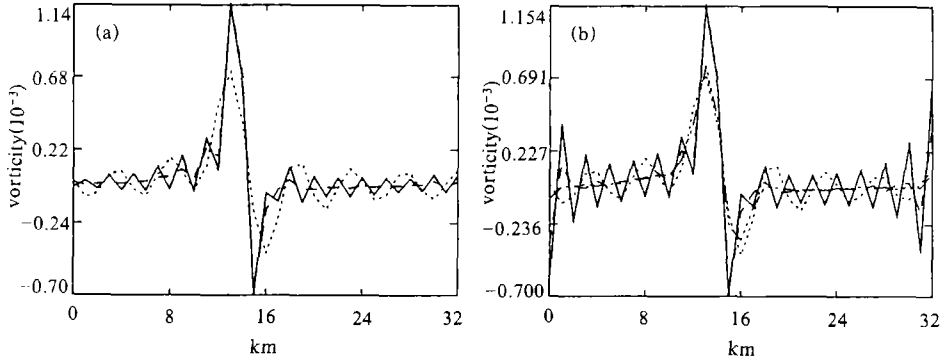


Fig. 4. Gibb's phenomenon and filtering. The solid line represents the original fields. The dotted line shows the result with 8th order ideal filter. The dashed line shows the result with the 8th order BW filter with waves truncated at wavenumber 15. (a) Vorticity field calculated by a spectral method; (b) As in (a) except for using Eq. (3), dash-dotted line shows the result with the 2th order BW filter with waves truncated of wavenumber 8.

order BW filter with truncation wave number equal to 8, a dotted line shows the result with 8-wave ideal filter, and dash-dotted line shows the result with the 2nd order exponential filter with truncation wave number equal to 6. The oscillations in Fig. 4a, show a typical Gibb's phenomenon introduced by an abrupt signal change without boundary trouble since model output is periodic in Cartesian coordinate. It is obvious that the oscillation amplitude is reduced with distance away from the area for sudden signal change. In Fig. 4b, Gibb's phenomenon is very strong, cause ripples in field, and also affect the amplitude of extreme. In addition to the above, it is obvious that Gibb's phenomenon can be introduced by sharp boundary effects where V_r and V_ϕ exhibit discontinuities for model output.

Figure 4 shows also results filtered by ideal, exponential and BW filters. The ideal filter is the least satisfactory. The effects of BW filter is somewhere between the ideal and exponential filters. At high orders, its features are close to exponential filter. Further details can be conveniently found in a general mathematical handbook.

The Gibb's phenomenon is a special feature when dealing with digital signals in the frequency domain. Near an abrupt change of a signal, very high frequency oscillations, with a large number of frequency components can be excited. For the signal we are processing, the rich frequency components are introduced through FFT due to the existence of boundaries and the rapid variations of the signal. Their amplitudes are dependent upon the level of the abruptness. Their relative magnitude will not be changed if a differentiation and convolution operations are not involved and the process is reversible, i. e. the original can be retrieved by inverse FFT. When differentiation and convolution operations are performed in frequency domain, they are applied not only to the frequency of the original field, but also to the spurious harmonics, including a variety of periods from low to high frequencies, i. e. their amplitudes are weighted by wave number. They change the wave number and dispersion results, such enormous amplitude is totally unexpected and the process is irreversible. A so-call coherence appears in real space with regular but complicated ripples that are superposed on the frequencies of the original field. Its complexity comes from the convolution operation of two functions in the wave number domain, which generates waves in sum and difference of the original frequencies. Any simple

modification of an individual wave will in general affect the entire output field. Their amplitudes change with the wave number of output field. Here, they influence the amplitude of almost every effective frequency of output, so that they can not be removed by conventional ideal filter. It is their impact upon every frequency component of the output field that makes the use of low order, low-pass BW or exponential filters more effective. This class of low-pass filter damps amplitudes of all frequencies with higher damping rate at higher frequencies. However, they still can not properly handle Gibb's phenomenon with excessive strength because excessive filtering will damp true signal to an unacceptable level (Fig. 4b).

Based upon the above analyses, the sudden jumps near the boundaries must be properly dealt with before reconstructing the wind field from the closure equation set.

3. Periodic Extension of Domain and Its Constraint

When deriving the closure equation by 2-D FFT, we not only assumed a wind field satisfying periodic boundary condition, but also implicitly accepted the condition that all the variables are periodic in both r and φ directions or x and y for Cartesian coordinates. In reality, this is not valid if a limited domain for variables is taken for analysis in actual wind fields. When an aperiodic function is transformed by the Fourier method, a large number of hamornics will appear due to the finite domain problem, which gives rise to deformation of the field pattern. To reduce the effect of aperiodic boundary, the domain is artificially extended (Fig. 3). In Figs. 5a—c, thick black line (bd) in middle of a curve represents original variable fields, dash-dotted line represents the extended domain. Other curves represent results in extended domain multiplied by the weighting functions. Figure 5a shows how the wind field data from 3-D cloud model is extended towards all sides (for clarity, only one line in the original field is drawn): ab is from cd, de is from bc. With this type of extension the cloud model output is made periodic in both x and y directions. Figure 5b shows other variable fields (e. g. radial velocity) extended; fixed b and d, ba and de is from bc and dc, respectively. Figure 5c shows another way of extending the domain of all variable fields including wind field. b and d extend only outwards. It is obvious that the method is most convenient for practical operation calculations. Hereafter, all the variables extended are multiplied by a special weighting function so that they converge at the boundaries to their mean values before the extension is made. It is very important that weighting function takes the specified form, which directly affects the results of boundary processing. The weighting function is defined as

$$W_F = \frac{1}{1 + (R/R_0)^{2N}}, \quad (7)$$

$$\text{where} \quad R = \sqrt{\left(\frac{r-r_0}{M}\right)^2}, \quad r_0 - \frac{M}{2} \leq r \leq r_0 + \frac{M}{2}, \quad (8)$$

$$\text{or} \quad R = \sqrt{\left(\frac{\varphi-\varphi_0}{K}\right)^2}, \quad \varphi_0 - \frac{K}{2} \leq \varphi \leq \varphi_0 + \frac{K}{2},$$

M and K are the lengths of the extended domain. r_0 and φ_0 is the center of the field (Fig. 3). R_0 is the truncated length. When $R = R_0$, $W_F = 0.5$. N is a weighting index. In Figs. 5a—c, three weighting curves correspond to $R_0 = 20, 24, 28$ and $N = 4, 6, 10$, respectively.

After this treatment, all the variables in the retrieval equation are assumed to satisfy the

periodic boundary conditions. Figure 5d shows the results of the extended domain technique applied to the retrieval of vorticity. The experiment results indicate that, when the parameters of the weighting function are properly selected ($N=6$, $R_0=30$ in our example), the same results can be obtained from the two boundary extension methods discussed above. It is seen from the figure that the boundary extension reduces the Gibb's phenomenon introduced by boundary problems; those introduced by abrupt signal change remain to be resolved by the filtering technique.

4. Simplification of Equations

After the data processing, the retrieval equation (6) can be solved in principle since its coefficient matrix is non-singular. It is, however, computationally expensive with little practical value in operational analyses. In fact, through detailed diagnoses it can be found that, except winds, the expression of many terms, such as Br , r^2 ... in the equation, take rather simple forms of function with apparent frequency pattern, and the corresponding spectral structure is usually a row or a column, mainly concentrated around the mean values. Among all the terms in the equation, the magnitude of the mean is at least two orders of magnitude bigger than other components. Therefore, all the other terms can be omitted to the first approximation in the left hand side of Eq. (6), except those with $(m-j=0, h-k=0)$ and $(j=0, k=0)$, which represent the contribution from the mean. Therefore, Eq. (6) can be written as

$$\begin{aligned} & \left[-r_{0,0} - iL_h \alpha B_{0,0} + (iL_h)^2 \alpha A_{0,0} - iL_m (rs)_{0,0} + i^2 L_m L_h \alpha (Br)_{0,0} \right] V_{\varphi m,h} + \left[-V_{m,k} \right. \\ & \quad \left. - iL_h \alpha B_{m,h} + (iL_h)^2 \alpha A_{m,h} - iL_m (rs)_{m,h} + i^2 L_m L_h \alpha (Br)_{m,h} \right] V_{\varphi 0,0} \\ = & - \sum_k iL_h r_{m-j,h-k} V_{r,j,k} + \sum_k \left[-iL_m L_h \alpha A_{m-j,h-k} + iL_m \alpha B_{m-j,h-k} \right. \\ & \quad \left. - (iL_m)^2 \alpha (Br)_{m-j,h-k} \right] (RV)_{j,k}. \end{aligned} \quad (9)$$

As the secondary approximation, same to the right hand side of Eq. (6) that can be written as follows

The left hand side of Eq.(9) equals:

$$\begin{aligned} & -iL_h r_{0,0} v_{r,m,h} + \left[-iL_m L_h \alpha A_{0,0} + iL_m \alpha B_{0,0} - (iL_m)^2 \alpha (Br)_{0,0} \right] (RV)_{m,h} - iL_h r_{m,h} V_{r,0,0} \\ & + \left[-iL_m L_h \alpha A_{m,h} + iL_m \alpha B_{m,h} - (iL_m)^2 \alpha (Br)_{m,h} \right] (RV)_{0,0}. \end{aligned} \quad (10)$$

The above equations are a set of simple linear equation. They are very easy to solve for all the Fourier coefficients of the tangential velocity, V_φ . Based on the retrieved tangential velocity, the divergence field and the vorticity field can be calculated conveniently.

5. The Summary of the Signal Processing Procedure Can Be Outlined as Follow

- (1) Set analysis region in polar coordinates.
- (2) Extend the analysis domain, from E, F, G, H in Fig. 3 to E', F', G', H'.
- (3) Calculate the known functions in the right hand side of Eq. (6).
- (4) Calculate the Fourier coefficient of V_φ based on Eq. (6).
- (5) Retrieve ζ and D according to the above V_φ .
- (6) Filter
- (7) Transform coordinates again for display by bilinear interpolation.

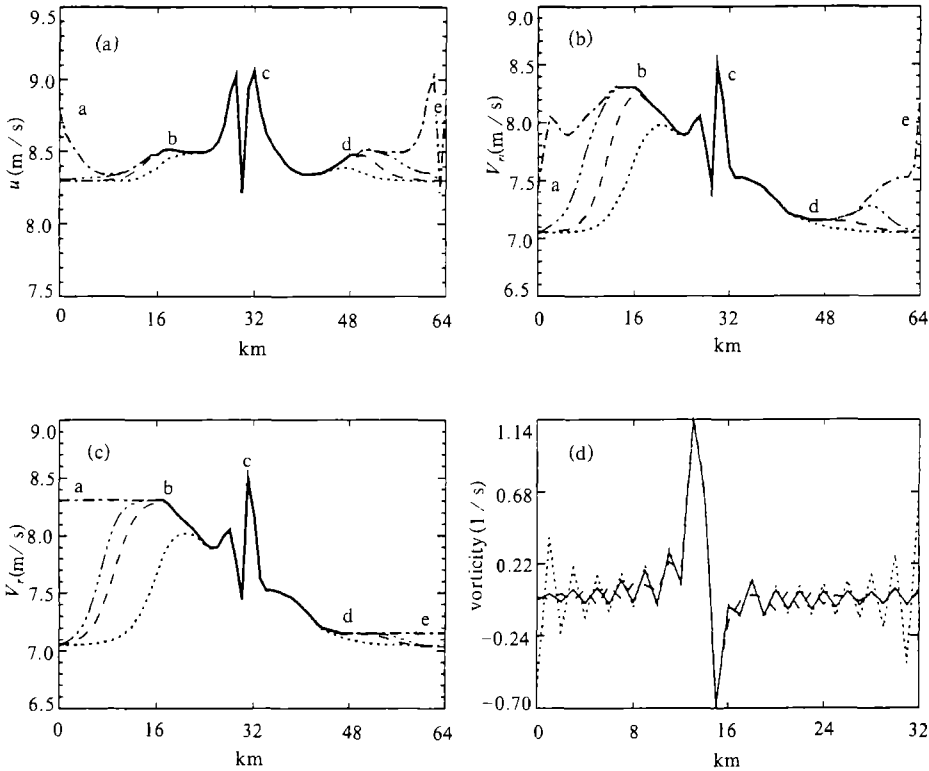


Fig. 5. Influence of domain extensions and weight functions. In Figs. a, b, c, the solid line in middle of curve represents original variable fields. Then dash-dot line represents the ways of extending domain. Other curves represent different weighting functions. (a) shows how extending u (v) components are extended; (b) and (c) show different ways of extending V_n ; (d) shows retrieved vorticity field (10^{-3}). Dash-dot line shows the extended domain, dashed line no extended and solid line shows original vorticity field.

V. RESULTS

1. Description of Experiments

Experiments have been performed to examine the performance and capability of the retrieval method. Details of the retrieval method are varied to test the algorithm's sensitivity under various circumstances, such as the presence of observational errors, missing observations, different combinations of domain and weighting functions, as well as variations in wind shear component and coefficient α in the conceptual model, etc. Due to the limitation of the computer core memory, Eq. (6) is solved in the domain bounded by the dashed lines shown in Fig. 1. ($20 \text{ km} \times 20 \text{ km}$) while Eqs. (9) and (10) are solved in the original $32 \text{ km} \times 32 \text{ km}$ domain. But the latter results are also shown in the $20 \text{ km} \times 20 \text{ km}$ domain in order to compare with the results from Eq. (6).

(1) The success of the retrieval is measured by RMS errors and the ratio of maximum of D , ζ and V_ϕ retrieved to that calculated by a spectral method and V_ϕ from the model output. The RMS errors are defined by

$$RMS = \left(\frac{\sum_{M,N} (F_r - F_c)^2}{M \times N} \right)^{\frac{1}{2}}$$

respectively. Here F denotes either divergence, vorticity or tangent velocity. The subscript r or c stands for the retrieved or 3-D model output fields respectively. M and N represent the number of the grid points in each of the directions.

(2) Observational errors were simulated by adding the actual value of V_r field at every grid point to the normal random error

$$V_r = V_r \times (1 + KE),$$

where V_r is the value of model output, E is a normally distributed random variable generated by the computer. When $K=0.1$ a 10% random error is added to the observations.

2. Experiments

Figure 6 represents the original fields at 3.75 km height from model output in polar coordinates corresponding to the area enclosed by the dashed lines in Fig. 1a which are calculated by a spectral method. Two criteria are used to measure the success of the retrieval: (a) the ratio of maximum value in the retrieval field to that in the model output and (b) the RMS error of the former. Note that the extreme values in Fig. 6 are weaker than the corresponding ones in Fig. 1. It is an inevitable outcome of using bilinear interpolation scheme to perform coordinate system transformation from the model Cartesian to polar since an extreme point in the Cartesian coordinates does not necessarily fall onto a grid point in the polar coordinate. We have no reason to expect the interpolated fields to show maximum or minimum values with same strength as the original fields. Our main concern here is to insure that the two grids have similar grid density, rather than conserve the extreme values during the grid transformation. The RMS error shown in the Fig. 6 is calculated from corresponding fields in the Cartesian coordinates.

In Table 1, "accurate" "app. 1" and "app. 2" correspond to retrieved values using Eqs. (6), (10) and (9) respectively. Experiment 1 is conducted under ideal conditions, that is, there are no observational or other errors, and the weighting function and the amount of the domain expansion is optimized. Radial velocities corresponding to the fields in Fig. 1 are located in the marked position ($OB' = 35$ km) on Fig. 3. Let us consider first the retrieval with $\alpha = 0.8 \times 10^5$ m s. U_z, V_z obtained from the convection model output:

$$U_z = 4.3 \times 10^{-3} \text{ s}^{-1},$$

$$V_z = 1.45 \times 10^{-3} \text{ s}^{-1}.$$

The amount of the domain expansion, $m = 22$ (each side); truncated length and weighting index in weighting function $R_0 = 3^\circ$, $N = 5$, respectively; grid size in φ direction, $jj = 45$. Figures 7 and 8 show the retrieved fields of D, ζ and V_φ from Eqs. (6) and (10), respectively. Comparing these to the actual fields shown in Fig. 6 (for space limitations, the retrieval results from Eq. (9) are not given here). We can see that all the results are quite good. The retrieved fields of D and ζ are essentially the same as those of the actual fields. The pattern of the retrieved V_φ is also in good agreement with Fig. 6c. Although the difference between the extreme values is significant, the

rate of change from the maximum to the minimum and the magnitude of the change are similar to those shown in Fig. 6, such that the retrieved fields of D and ζ with higher quality can be obtained. The V_ϕ field in Fig. 7c is not quite ideal, with smaller values at the top-left and the right bottom corners. This is because the imposed periodic boundary condition in the finite domain results in a deformation of model mean winds in the process of solving the retrieval equation. This phenomenon is not clear in Fig. 8c, but does exist (figures not shown). The weaker deformation is due to the fact that Eqs. (9) and (10) are solved in the $32\text{ km} \times 32\text{ km}$ domain, but only a portion of the solution, containing the disturbances, is shown here. It is also seen in this experiment that the magnitude of the retrieved D field is close to that of the original D field, while the magnitude of the ζ field is smaller than that of the original ζ field. Although their magnitudes are somewhat smaller, the difference among the patterns is quite small, with Eq. (6) the best and Eq. (10) the worst. A closer look at the figures makes it clear that the centers of vorticity and divergence have been rotated by a very small angle during the retrieval process. It is apparent that the conceptual model is not in total agreement with the wind from the 3-D model output.

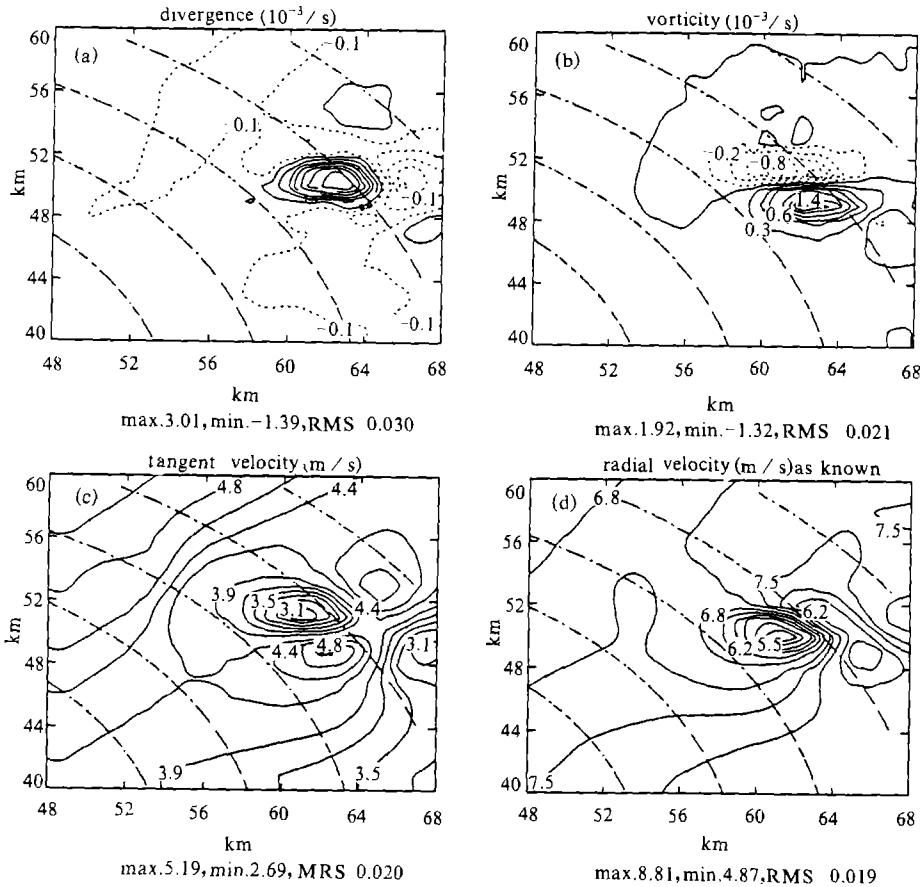


Fig. 6. Original fields at 3.75 km height from model output in polar coordinates.

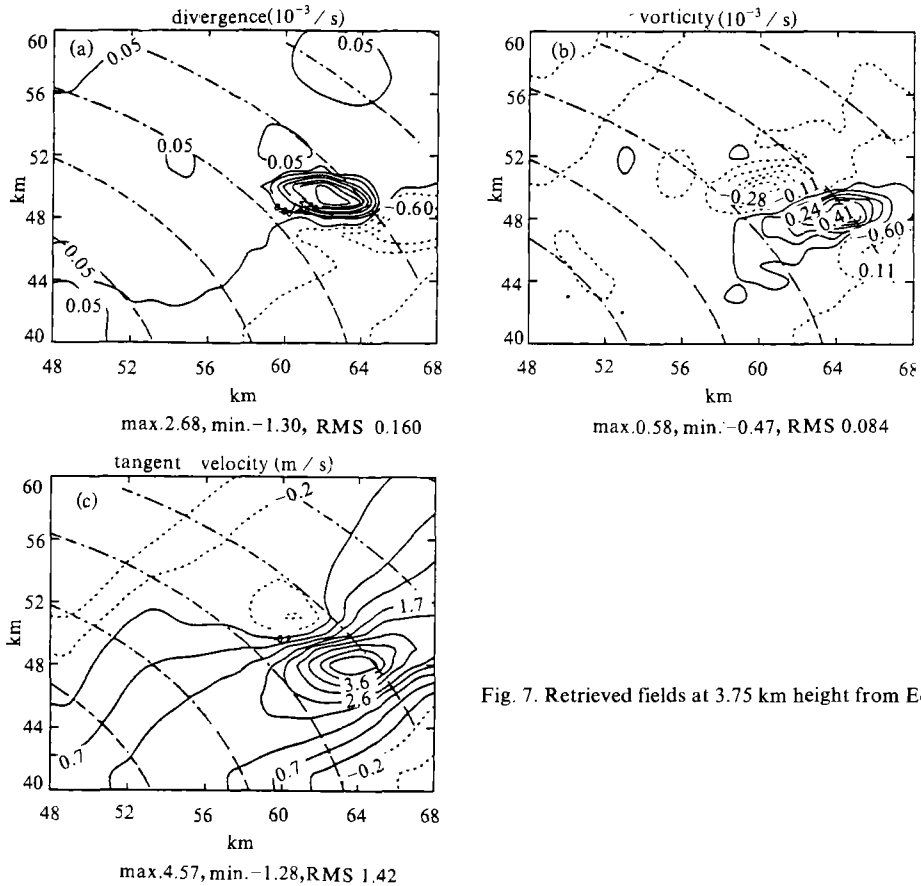


Fig. 7. Retrieved fields at 3.75 km height from Eq. (6).

All the following experiments were conducted with smoothing in space except experiments 5 and 6. All the smoothing was performed directly upon the retrieved V_φ , D , ζ fields. In experiments 2 and 3 the sensitivity of the retrieval algorithm to observational errors, is examined. The errors were simulated by adding a normally distributed random error to the actual field of V_r . A 5% random error was added to each gridpoint value in experiment 2 and 10% error was added in experiment 3. In these two experiments the deformation of the V_φ , D , ζ fields, retrieved by three different methods, is very small after the spatial smoothing.

Besides the convolution smoothing listed in the table, the median smoothing and the mean smoothing have also been tested. The extreme values obtained from these methods are much smaller than those of the original fields, and the patterns are distorted to different extents. With properly chosen weighting coefficients of the convolution smoothing, not only can the pattern of the retrieved field be closer to that of the original one, shown in Fig. 6, but also the extreme values be kept close to actual values.

In experiments with 15% observation errors, the patterns of D and V_φ fields are still clearly recognizable from the background noise while that of ζ field is completely buried by the latter, although the same smoothing is applied to all the fields. It is seen that with stronger amplitude of the original fields, their ability to resist the interference of noise is improved.

Table 1. Summary of Statistics

Description of experiment		App. 1		App. 2		Accurate	
		Ratio of max. RMS		Ratio of max. RMS		Ratio of max. RMS	
① V_r data at 3.75 km height, $\alpha = 0.8 \times 10^5$	D	0.85	0.154	0.88	0.158	0.89	0.160
	ζ	0.25	0.097	0.24	0.074	0.30	0.084
	V_φ	0.85	1.362	0.86	1.402	0.88	1.420
② Same as ① except with 5% obs. error	D	0.83	0.123	0.81	0.112	0.82	0.110
	ζ	0.24	0.126	0.21	0.101	0.26	0.098
	V_φ	0.72	1.630	0.87	1.430	0.87	1.501
③ Same as ⑤ except with 10% obs. error	D	0.72	0.174	0.80	0.140	0.80	0.153
	ζ	0.22	0.185	0.20	0.143	0.23	0.161
	V_φ	0.71	1.753	0.79	1.624	0.81	1.731
④ Same as ① except with 50% shear error	D	0.79	0.138				
	ζ	0.33	0.100				
	V_φ	0.79	1.379				
⑤ Same as ② except with -50% shear error	D	0.93	0.187				
	ζ	0.16	0.097				
	V_φ	0.92	1.368				
⑥ Same as ① except with $U_z \times 2.5$	D	0.77	0.136				
	ζ	0.58	0.126				
	V_φ	0.82	1.389				
⑦ Same as ② except with $V_z \times 3.5$, $U_z / 3.5$	D	0.77	0.136				
	ζ	0.29	0.069				
	V_φ	0.75	1.415				
⑧ Same as ① except with $\alpha = 0.0$	D					1.60	0.935
	ζ						
	V_φ					1.08	1.998
⑨ V_r with 1/2 resolution	D	0.71	0.249				
	ζ	0.11	0.180				
	V_φ	0.76	1.970				
⑩ 0.1×1 gridpoint hole in obs.	D	0.62	0.430				
	ζ	0.10	0.161				
	V_φ	0.58	1.710				

As indicated by above experiments, the solution of Eq. (10) with 10% observation errors is also very close to that of Eq. (6); therefore, all the following experiments have been only conducted by app. 1 (accurate run takes over 240 times of CPU on SUN workstation, than app. 2 run does). The results are listed in Table 1.

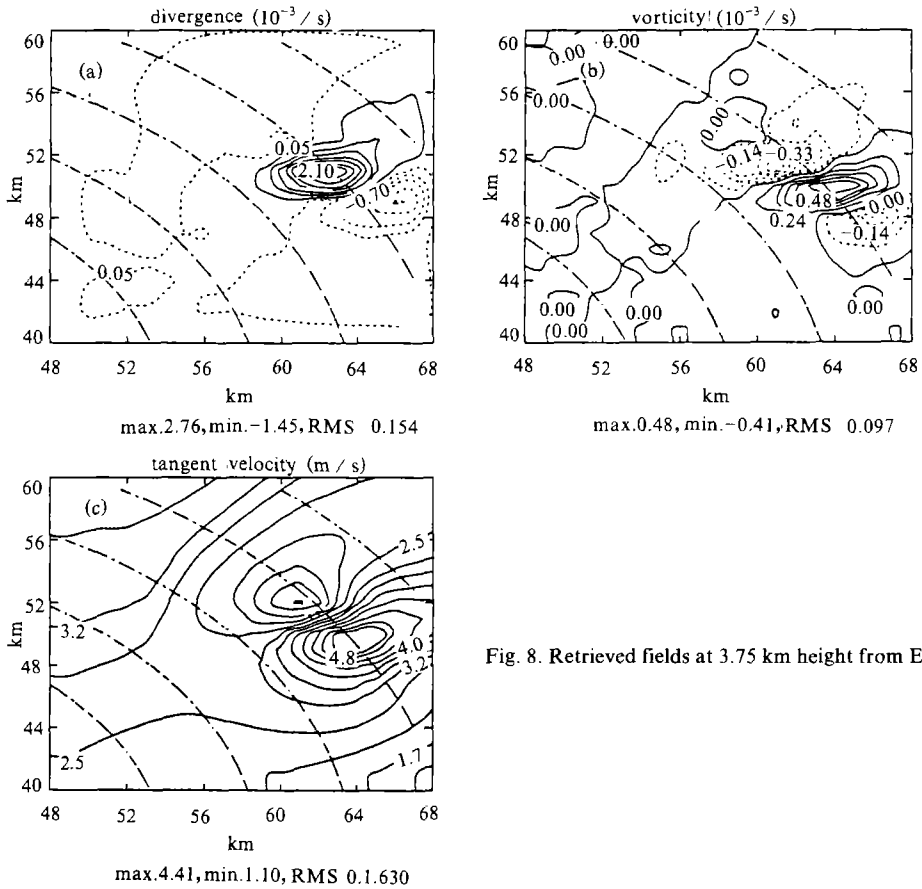


Fig. 8. Retrieved fields at 3.75 km height from Eq. (10).

Experiments 4, 5, 6 and 7 are designed to test the sensitivity of the basic variables retrieved to the errors of horizontal wind shear. Comparing the listed values in Table 1 with that of experiment 1, we can see that the retrieved D , ζ and V_ϕ in the set of experiments are almost as good. The RMS errors in D , ζ and V_ϕ are very close to that in experiment 1. In experiment 4, extreme values of D and V_ϕ are reduced to about 10% of the value shown in Fig. 6, while that of ζ field is increased to about 10%. Unlike experiment 4, in experiment 5, extreme values of D and V_ϕ are increased to about 10%, while that of ζ field is reduced to about 10%. In experiments 6 and 7, we can see the sensitivity of the fields retrieved to errors in horizontal wind shear direction.

The pattern of the field retrieved from experiment 7 is the best of all the experiments. The rotation of the centers of vorticity and divergence produced by the retrieval process has disappeared. Since the patterns of the retrieved fields are similar to those in Figs. 7 and 8, the retrieved fields are not shown in the experiments.

Experiment 8 tests the performance of the retrieval process with $\alpha = 0$ in Eq. (6). The experiment is the same as experiment 1 except that the coefficient is set to zero in the retrieval equations. When $\alpha = 0$, the retrieval equation (6) is greatly simplified

$$-\frac{\partial(rV_\phi)}{\partial r} + \frac{\partial V_r}{\partial \phi} = 0,$$

rV_ϕ is considered as unknown here, so that the complicated convolution operations can be avoided and no coupled multi-variable equation need to be solved. Of particular interest is that $\alpha=0$ implies an irrotational flow. Since the model ζ field is close to $2/3$ of the D field in magnitude, it is not too surprising to find the field of divergence to be not too sensitive to the assumption $\zeta=0$. In this experiment, although the retrieved D pattern is reasonable after the filtering, the retrieved ζ pattern using $\zeta=0$ is not that realistic, with an obvious deformed wave structure (not shown), which cannot be corrected by proper filtering. The widely used linear wind assumption implies irrotational flow. It is seen from this example that for real winds with $\zeta \neq 0$, it is very difficult for the linear wind assumption to retrieve V_ϕ field with high quality. It is true at least in the examples we have studied.

Figure 9 shows the correlation coefficient between the actual and retrieved divergence fields for a wide range of α . As expected the maximum value of ρ is obtained at the true value of $\alpha=0.8 \times 10^5$ m s. However, there is a wide range of α within which the pattern of divergence is well retrieved. When $\alpha > 3$, the pattern of vorticity field is deformed extremely.

In experiment 9, observations from every other gridpoint were skipped reducing the resolution in each direction by half. Experiment 10 tests the effect of a 1×1 gridpoint hole in the data. It is seen from Table 1 that all three retrieved fields show relatively large RMS error.

For the strong convective cells of special interested in the present study, the observed V_r should not have large amount of missing points if the retrieval method is to produce good results. Missing data could be filled with information obtained by interpolation methods. Figure 10 shows as a function of grid density in the polar coordinates the change of RMS errors of D and ζ fields retrieved using Eq. (9). If the grid density in the polar coordinates is 50% lower than that in the model, RMS error increases significantly. In practice, the grid density in polar coordinates depends upon antenna beam width in azimuth and the distance from the convective cells to the radar station. The characteristics of the convective cells can be properly retrieved only when their spatial features are properly sampled.

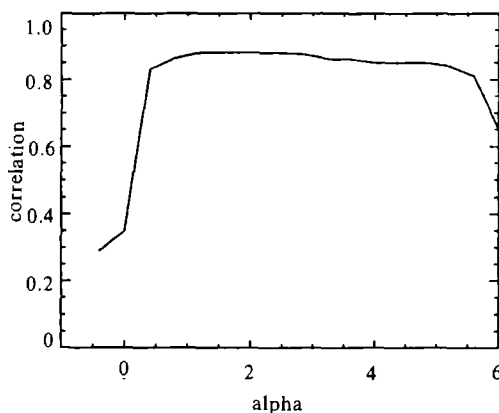


Fig. 9. Influence of the choice of alpha on the retrieval of the field of divergence.

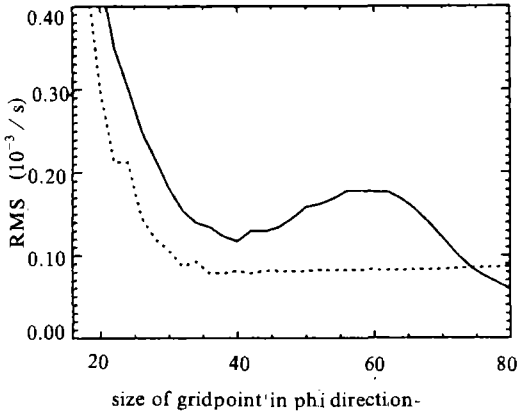


Fig. 10. RMS error (s^{-1}) in the retrieved ζ (dotted line) and divergence (solid line) as a function in phi direction

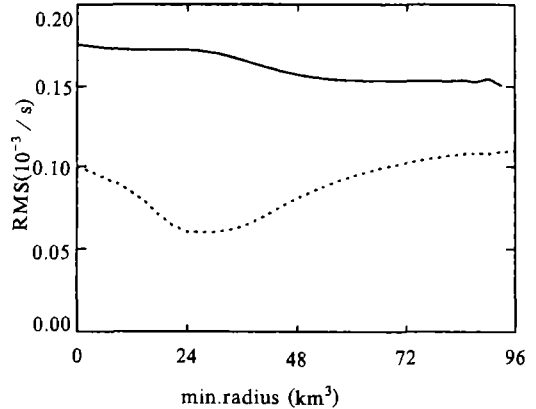


Fig. 11. RMS error (s^{-1}) in the retrieved ζ (dotted line) and divergence (solid line) as a function in min. radius.

Figure 11 shows the RMS errors of D and ζ (retrieved using Eq. (10)) as a function of distance OB' shown in Fig. 3. The curve is nearly horizontal and therefore, the solution of Eq. (10) is almost independent of the distance, except the RMS error is slightly greater when the distance is small.

VI. SUMMARY AND CONCLUSIONS

For a strongly convective cell, when an intense vertical shearing occurs in horizontal wind field in the environmental background, the convergence updraft column becomes inclined. For this method for finding the horizontal wind perturbation fields from a single velocity component field has been developed and tested. A semi-quantitative conceptual model, based on the relationship between kinematic properties within convective flows, was used for the retrieval of horizontal wind perturbation fields from single Doppler velocities.

A set of experiments has been performed to test the performance of the method, using a 3-D convection model as a test bed. The flow simulated by the model provided data for this study. Main conclusions are as follows:

(1) The position of a strongly convective cell is first located by using the PPI and RHI scanning, and then the vertical shearing of the horizontal windfield is calculated by means of the VAD detection scheme to make preprocessing of the data, with which the domain is determined that answers roughly the purpose of the conceptual model.

(2) Given complete observations of a single Doppler velocity component, in regions where the conceptual model holds, the other velocity components can be satisfactorily retrieved with a reasonable amount of computing effort. Although two peak values in the retrieved V_φ and ζ fields show relative amplitudes different of those in the original ones, their overall structures are still identical without significant distortion. The conservation of wind pattern is an important result in mesoscale weather analysis and prediction.

(3) The spatial distribution of retrieved divergence is not too sensitive to the degree in which the conceptual model holds. Even if a completely irrotation flow is assumed the pattern of

retrieved divergence is reasonably well correlated with the actual field, though the values are overestimated. The field whose magnitude is largest is better retrieved when other fields are set as zero.

(4) The following procedure is taken:

- i) extend the domain;
- ii) multiply the wind component by the weighting function to control the boundary problem;
- iii) solve the closed equation set for the finite domain with periodic boundary condition using FFT technique, filtering.

This procedure is feasible. Although the mean value of the retrieved V_ϕ field is modulated by the azimuth angle, its influence on the perturbation fields of D and ζ , calculated from the retrieved V_ϕ , is minor and negligible.

(5) In principle, contribution from every spectral line of a variable must be considered to obtain exact retrieved fields. In our practice, however, based on the spectral structure of the variables in Eq. (6), a variable with simple structure is replaced by its mean values which has largest amplitude among the spectral lines; whereas a complicate variable, such as V_ϕ or V_r , keeps contributions from all its spectral lines. Eq. (9) thus obtained processes a solution that is very close to the solution of Eq. (6). The solution of Eq. (10) is also very close to that of Eq. (6). Although ζ field is smaller in amplitude, this reasonable simplification makes our retrieval method be of practical value in operation analyses. In particular, the solution of Eq. (10) requires very little computer time, such that it is convenient for quasi-real time processing.

(6) The algorithm can tolerate random observational errors at least up to 10% of the observed magnitude. Generally, as the amount of the observations decreases, the performance of the retrieval is degraded. However, the missing observations can be compensated by the space smoothing constraint.

In our best effort, we have considered the use of real data in this method to retrieve the perturbation field, but problems remain. Although, the amount of computation of the retrieval method needed does not restrict its practical application, the adjustment of the functional relationship to the observations sets a limit to the area over which the method can be applied with sufficient precision. A different functional assumption could be more adequate. Nevertheless, the approach presented here seems very promising and should be further explored in the future studies.

We wish to express our gratitude to Dr. Tian Sheng for help in discussing and to Claude Desrochers for help with the computing programs.

REFERENCES

- Gu Songshan et al. (1986), Digital terminal of 713 radar, *J. Nanjing Ins. Meteor.*, **9**: 403—411.
- Johnston, B. W. and Marwitz, J. D. (1990), Single-Doppler radar analysis of banded precipitation structures, *J. Atmos. Oceanic Technol.*, **5**: 100—148.
- Laroche, S. and Zawadzki, I. (1988), Retrieval of horizontal wind field from single Doppler observations, *Proc. Weather Radar Conf. 24th*.
- Lilly, D. K. (1986), The structure, energetics and propagation of rotating convective storm—Part 1: Energy exchange

- with mean flow, *J. Atmos. Sci.*, **43**: 113—125.
- Passarelli, R. E. (1983), Wind field estimation by single Doppler radar techniques, *Preprints, 21st Conf. on Radar Meteorology*, pp. 526—529.
- Ray, P. (1976), Vorticity and divergence fields within tornadic storms from dual Doppler observation, *J. Appl. Meteor.*, **15**: 879—890.
- Sun Juazhen et al. (1991), Recovery of three-dimensional wind and temperature fields from simulated single-Doppler radar data, *J. Atmos. Sci.*, **4(B)**: 876—889.
- Tuttle, J. P. and Foote, G. B. (1990), Determination of the boundary layer radar, *J. Atmos. Oceanic. Technol.*, **5**: 218—232.
- Yan, M. K. and Michaud (1982), Numerical simulation of a cumulus ensemble in three dimensions, *J. Atmos. Sci.*, **39**: 1062—1079.
- Zawadzki, I. I. (1973), The loss of information due to finite sample volume in radar-measured reflectivity, *J. Appl. Meteor.*, **12**: 683—687.